Pulse Testing for Monitoring the Thermal Front in Aquifer Thermal Energy Storage

Peter A. Fokker[a,b,c], Eloisa Salina Borello[a,*], Dario Viberti[a], Francesca Verga[a], Jan-Diederik van Wees[b,c]

[a] *Politecnico di Torino, Turin, Italy*
[b] *TNO – Geological Survey of the Netherlands, Utrecht, the Netherlands*
[c] *Utrecht University, Utrecht, the Netherlands*

ABSTRACT

Seasonal storage of heat in shallow aquifers for increasing the efficiency of geothermal energy systems requires a proper monitoring strategy. We expanded our earlier work on harmonic pulse testing (HPT) to incorporate the effect of a temperature front moving into the reservoir due to injection of hot (or cold) water. Our analytical solutions were applied to monitor the thermal front evolution in a doublet system. Thermal front position and average temperature around the injector could indeed be characterized through the application of the proposed HPT interpretation. Additional analyses were carried out adding noise to evaluate the robustness of the interpretation methodology.

1. Introduction

The development of Geothermal Energy in the Netherlands is mainly associated with heating. However, traditional geothermal doublets cannot operate at their optimal power due to climate seasonality and the daily fluctuations in weather and heat demand. The economics of geothermal heat could therefore be enhanced considerably by storage that evens out heat surplus and heat demand. One of the storage possibilities currently considered is seasonal storage of heat in shallow aquifers: ATES (Aquifer Thermal Energy Storage). It would store the surplus of energy supply in the summer and harvest it in the winter. This strategy potentially increases the overall efficiency of the system.

The efficiency of an ATES system depends on the ability to recover the stored heat. Recovery depends on the distribution of reservoir properties and on the operational design. However, the geological setting, including heterogeneities in the reservoir properties, is often poorly known. Further, the resulting temperature distribution is subject to uncertainty both after injection and after production. As a result, an understanding of the heat distribution is key for being able to optimize the operational efficiency. Effective monitoring of the heat distribution upon injection and production of hot and cold water is thus mandatory.

Well testing is an important technique for the determination of reservoir properties, including flow boundaries and mobility interfaces

(Gringarten, 2008). Proper production/build up testing, however, requires an initial well shut-in to approximate pressure equilibrium minimizing effects of pumping operations, and a well shut-in during the build-up (Bourdet 2002). Moreover, to be interpretable, the registered pressure should not be influenced by activity in neighboring wells, therefore a test usually involves also a temporary interruption of nearby operations. Periodic Pumping testing (Renner & Messar, 2006) also referred to as Harmonic Pulse Testing (HPT) in the reservoir engineering literature (Hollaender et al., 2002), on the contrary, is applicable during ongoing operations and does not require significant alteration of tested well net production/injection (Salina Borello et al., 2017). Furthermore, it does not require special equipment: the standard well testing equipment is sufficient, provided that well-defined rate pulses are imposed and precise pressure monitoring is carried out.

In the present contribution, we extend the pulse testing methodology to the monitoring of thermal zones around a geothermal injector well or to the monitoring of a thermal energy storage system. We will apply the interpretation approach presented by Fokker et al. (2018) that is based on the strong similarity existing between the derivative of the harmonic response function versus the harmonic period and the pressure derivative versus time, typical for production/build-up well testing. After detailing the theoretical basis, we will demonstrate the applicability of HPT to thermal front monitoring through the application of the developed analytical solution in the frequency domain to the

Nomenclature

ϕ	porosity	p_{res}	reservoir pressure
μ	viscosity	p_{well}	well pressure
ω	angular frequency ($= 2\pi/T$)	P_D	dimensionless pressure
λ	mobility	P_D'	dimensionless pressure derivative
η	diffusivity	p_ω	pressure harmonic component
ζ	multiplier associated to diffusivity	q	volumetric rate
C	wellbore storage	q_{perfs}	volumetric rate actually filtrating from the well
C_K, C_I	coefficients multiplying Bessel functions K and I respectively	q_{well}	imposed volumetric rate at reservoir conditions
c_f	formation compressibility	q_ω	rate harmonic component
c_t	total compressibility	r_{eq}	equivalent radius of front position (numerical simulation)
c_w	water compressibility	r_1	fluid front position between inner and outer zone (radial composite model)
f	frequency	r_w	well radius
g_ω	time-independent part of harmonic pressure component	R	pressure-rate ratio of harmonic components
h	net pay	$|R|$	amplitude of R
i	complex unit	$|R'|$	amplitude of derivative of R with respect to $\ln(1/f)$
I_0, I_1	modified Bessel functions of the first kind	S	skin
k	reservoir permeability	t_D	dimensionless time
k_h	horizontal permeability	T	oscillation period
k_z	vertical permeability	T_f	fundamental oscillation period
K_0, K_1	modified Bessel functions of the second kind	T^*	critical oscillation period
M	mobility ratio	T_D	dimensionless oscillation period
P	pressure	T_1	temperature of the inner zone (radial composite model)
		T_m	median temperature of heated zone (numerical simulation)

interpretation of synthetic data generated through analytical and numerical models. As a first step, we will assess the monitoring feasibility of the thermal front of a geothermal doublet system. In this case, synthetic pressure data at the injector are generated analytically by mimicking the presence of a cooled zone through a radial composite model. Then, we will demonstrate the feasibility of the technique in monitoring the heated zone extension in an ATES scenario using a commercial numerical simulator, to overcome the hypothesis of axial symmetry and a step function for the temperature change. Realistic thermal front evolution and the corresponding pressure measurements at the heat storage well were generated, taking into account thermal convection and conduction and production and injection histories of the two wells. Synthetic well pressure measurements were then interpreted adopting our analytical models in the frequency domain, obtaining a reliable characterization of heated zone in terms of median temperature and equivalent radius.

2. Materials and Methods

2.1. Harmonic Pulse Testing

The concept of Harmonic Pulse Testing was first proposed by Kuo (1972) and has been developed for the determination of hydraulic parameters by several authors (Black & Kipp, 1981; Cardiff & Barrash, 2015; Despax et al., 2004; Hollaender et al., 2002), in different scenarios like two-phase flow (Fokker & Verga, 2011; Zhou & Cardiff, 2017), fractured wells (Morozov, 2013; Vinci et al., 2015), fractured reservoir (Guiltinan & Becker, 2015), gas wells (Salina Borello et al., 2017), and horizontal wells (Fokker et al., 2018). It was also suggested for the characterization of heterogeneous reservoirs (Ahn & Horne, 2010; Cardiff et al., 2013; Copty & Findikakis, 2004; Fokker et al., 2012; Rosa & Horne, 1997), fault hydraulic properties (Cheng & Renner, 2018), and leakage from faults (Sun et al., 2015). Some real applications of HPT have been documented in the literature for heterogeneity detection in aquifers (Renner & Messar, 2006; Fokker et al., 2013; Cardiff et al., 2019); single and multilayer reservoirs (Rochon et al., 2008); a gas storage field confined by a lateral aquifer (Salina Borello et al., 2017), a horizontal well in a gas storage field (Fokker

et al., 2018) and a geothermal system (Salina Borello et al., 2019).

Harmonic Pulse Testing imposes the regular alternation of two rate values in a well, called Pulser. Combinations of different productions and/or injections or production/injection alternated with well shut-in, are possible. The effect is a pressure response that is also periodic. Then, the harmonic components in both the rate and the pressure are determined through Fourier analysis, possibly preceded by pressure detrending (Viberti, 2016; Viberti et al., 2018). The pressure-rate relationship depends on the physics of the reservoir response and the parameters in the physical correlations. When the proper models are used, interpretation of the measured pressure response through an inversion or parameter estimation technique can be applied to derive the reservoir properties.

A great advantage of HPT is that it requires neither the initial static conditions (well shut-in of the tested well), nor the shut-in of any neighbor wells during the test. Under the assumption of linearity, the pressure and flow solution of a reservoir with many wells and changing production rates can then be added to the solution of the harmonic test. A Fourier transformation will provide the signal components corresponding to the imposed frequencies. Furthermore, there will be no frequency mixing; frequencies can be treated independently.

We present the equations for a composite radial system, which is the approximate model for an ATES storage well that is surrounded by a region of altered temperature. In a reservoir containing single-phase slightly compressible fluid, the flow is described by the equation:

$$\phi c_t \rho \frac{\partial p}{\partial t} = \nabla \bullet [\lambda \rho \nabla p] \tag{1}$$

Where $\lambda = k/\mu$ is the mobility; ϕ is the rock porosity, c_t is the total compressibility ($c_t = c_w + c_f$ where c_w is the compressibility of the water and c_f is the compressibility of the formation), k is the rock permeability, μ is the fluid viscosity, ρ is the fluid density, p is the pressure and t is the time.

When a piecewise homogeneous domain is assumed with approximately constant density, the equation (1) is linear and can be locally solved analytically. We obtain:

$$\frac{\partial p}{\partial t} = \eta \nabla^2 p \tag{2}$$

where $\eta = \lambda/\phi c_t$ is the diffusivity constant. We consider each frequency component independently because they can be isolated through Fourier transformation as noted above. We apply a harmonic injection rate:

$$q_{well} = q_\omega e^{i\omega t} \tag{3}$$

Eq. 3 is equivalent to $q_{well} = q_\omega(\cos(\omega t) + i\sin(\omega t))$. Thus, the real part of q_{well} represents a (co)-sinusoidal or harmonic test. We write the pressure solution for each frequency as a complex-valued function that is the product of a space-dependent and a time-dependent function:

$$p_\omega(\mathbf{r}, t) = g_\omega(\mathbf{r})e^{i\omega t} \tag{4}$$

The angular frequency is defined as $\omega = 2\pi/T$, where T is the cycle time of the imposed harmonic signal. This results in a time-independent differential equation for g_ω:

$$i\omega g_\omega(\mathbf{r}) = \eta\nabla^2 g_\omega(\mathbf{r}) \tag{5}$$

For a reservoir with radial symmetry, the diffusivity equation can be rewritten into radial coordinates. We obtain:

$$i\omega g_\omega(r) = \eta\frac{1}{r}\frac{d}{dr}\left(r\frac{dg_\omega}{dr}\right) \tag{6}$$

The general solution to this equation is a superposition of two modified Bessel functions of order 0 (K_0 and I_0) (Abramowitz & Stegun, 1964). For convenience, we scale the solution by the injection rate amplitude q_ω, and we write the general solution as:

$$g_\omega(r) = q_\omega C_K K_0(\zeta r) + q_\omega C_I I_0(\zeta r) \tag{7}$$

where

$$\zeta = \sqrt{\frac{i\omega}{\eta}}$$

and C_K and C_I are free parameters to be determined by imposing boundary conditions. The Bessel functions have a complex argument since the differential equation has a complex parameter. As a result, the solution is complex as well, and has an amplitude and a phase when translated to the real domain. At the wellbore, pressure must be corrected to include skin effect (S) as shown in detail in Appendix A.

We consider a composite system of two concentric zones around the wellbore with different temperatures (in the literature also referred to as concentric-shell model (Cheng and Renner, 2018)). The applicability of this sharp-front approximation for the actual case with a continuously changing temperature will be assessed later. Different temperatures imply different fluid viscosities and possibly different compressibilities. Therefore, the mobility (λ), the diffusivity (η), and the associated multiplier (ζ) for the radial distance is different in the two zones. The pressure expression is thus characterized by 4 free parameters (C_K^i and C_I^i for each zone i), whose determination requires 4 conditions. These are given by two boundary conditions (reservoir inflow from the wellbore corrected for wellbore storage (C); vanishing pressure disturbance at infinity) and two continuity conditions at the interface between the two zones (continuity of pressure and flow rate). The evaluation of the parameters for the composite radial system is provided in Appendix B. The parameters and Bessel function evaluations depend on the reservoir and fluid parameters, the fluid front position, and the frequency. From the resulting pressure expression, we can determine a response function for every harmonic component of the injection or production rate tested:

$$R_\omega^{pulser} = \frac{p_{well}}{q_{well}} = C_K^1 K_0(\zeta_1 r_w) + C_I^1 I_0(\zeta_1 r_w)$$
$$+ S\zeta_1 r_w [C_K^1 K_1(\zeta_1 r_w) - C_I^1 I_1(\zeta_1 r_w)] \tag{8}$$

For an observer well, the expression of the response function depends on its position with respect to the thermal front (i.e. observer well inside or outside the altered temperature area):

$$R_\omega^{obs} = \frac{p_{obs}}{q_{well}} = \begin{cases} C_K^1 K_0(\zeta_1 r_{obs}) + C_I^1 I_0(\zeta_1 r_{obs}) & (r_{obs} < r_1) \\ C_K^2 K_0(\zeta_2 r_{obs}) & (r_{obs} \geq r_1) \end{cases} \tag{9}$$

Derivation details for eq. (8) and eq. (9) are given in Appendix B.

2.2. Interpretation Methodology of Harmonic Pulse Testing

For the HPT interpretation, we focused on the response of the pulser well because we observed that the pulser response (R_ω^{pulser}) was significantly more sensitive to variations of the heated zone than the observer response (R_ω^{obs}). Thus, eq. 8 represents the analytical solution that will be employed as interpretation model. Interpretation is the process of matching test data through selection of the interpretation model (radial composite, Infinite Acting Radial Flow, etc.) and characterization of model parameters. In eq. 8, C_K^1, C_I^1 and ζ_1 depend on the reservoir and fluid parameters, fluid front position and frequency. Both amplitude ($| R_\omega^{pulser} |$) and phase shift ($\angle R_\omega^{pulser}$) were analyzed.

Data need to be preprocessed before interpretation because the model is in the frequency domain. To this end, rate and well pressure data are transformed through FFT obtaining Q_ω and P_ω, respectively, which represent the signal value of each frequency component f = ω/2π. The penetration depth decreases with increasing frequency (Fokker et al., 2018). Amplitude peaks, representative of the harmonic components, are identified in the flow rate and pressure spectra and the response function is calculated as the amplitude ratio $R_\omega = P_\omega / Q_\omega$, for each frequency component. The derivative of the amplitude ratio with respect to the logarithm of the oscillation period (R') is calculated by a three point data differentiation algorithm (Bourdet, 2002). Then, the modulus of harmonic response function (|R|) and the modulus of its derivative (|R'|) versus the harmonic period (T) are plotted on a log-log scale allowing an interpretation analogous to conventional Pressure Transient Analysis (Bourdet et al., 1983; Gringarten et al., 1979). Flow geometries and flow regimes can be easily identified on the derivative plot. In particular:

- |R'| showing a plateau (linear trend with slope 0 called horizontal stabilization in the Pressure Transient Analysis terminology) corresponds to Infinite Acting Radial Flow. The stabilization value, i.e. the ordinate value of the trend (y_M), is proportional to the investigated zone properties (Fokker et al. 2018):

$$k = \frac{B\mu}{4\pi h}\frac{1}{y_M} \tag{10}$$

If the aquifer contains two zones characterized by different viscosities, two different horizontal stabilizations should be visible (Fig. 1). For the injector of a geothermal doublet, the undisturbed zone is the outer one. Thus, the mobility of the system can be estimated from that stabilization.

- The ratio between the values corresponding to the two horizontal stabilization gives the mobility ratio (M) between inner (1) and outer zone (2):

$$M = \left(\frac{k}{\mu}\right)_1 / \left(\frac{k}{\mu}\right)_2 \tag{11}$$

- The critical oscillation period T* corresponds to the transition between the two zones with different mobility and can be picked up from log-log plot visual inspection (Fig. 1). This allows to estimate the position of the front (r_1):

$$r_1 = 1.5\sqrt{\frac{kT^*}{2\pi\mu c_t\phi}} \tag{12}$$

- At high frequency, corresponding to the investigation of the near wellbore area, |R| and |R'| both show a linear trend with a unit slope
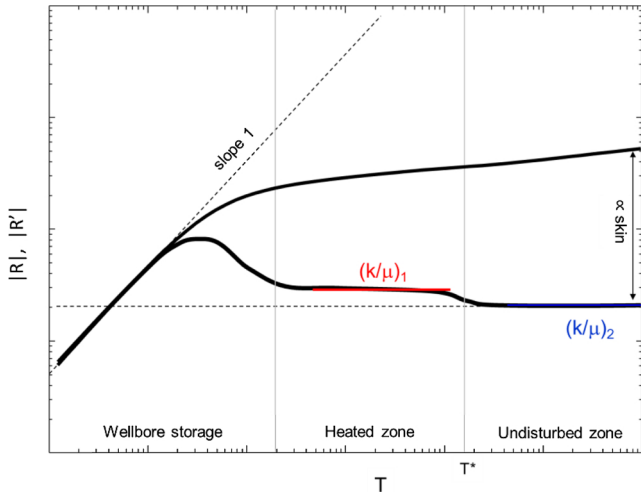
Fig. 1. Schematic of HPT log-log plot for a radial composite model of aquifer (M = 0.66).

on the log-log plot when wellbore storage occurs (Fokker et al. 2018), i.e. when the pressure response is dominated by the compression and expansion of the fluid in the well. Such phenomenon is more severe if the well volume (V) and the fluid compressibility (c_w) are large. However, the wellbore storage can be non-negligible also in geothermal aquifers (Salina Borello et al., 2019). By selecting the match point (x_M, y_M) at the intercept of the first horizontal stabilization and the linear wellbore storage trend, we can quantify the wellbore storage as:

$$C = V c_w = 2 x_M \frac{kh}{\mu} = \frac{B}{2\pi} \frac{x_M}{y_M} \qquad (13)$$

- The distance between |R| and |R'| on log-log plot is proportional to the well damage (skin), which is responsible for an additional pressure drop at the wellbore.

The |R| and |R'| data points vs. oscillation period are represented on a log-log plot, while phase shift (∠R) vs. oscillation period is represented on a semilog plot; both are compared with an analytical interpretation model obtained for a given combination of model parameters values. Similarly to conventional Pressure Transient Analysis, the values of model parameters are modified, in a trial and error process, in order to obtain an acceptable match of the real data. The quality of the match is typically based on visual inspection. This trial and error procedure is guided by identification of the match point, the two horizontal stabilizations and the transition between them (eq. 10–13).

Assuming the permeability to be constant, M represents the ratio between viscosities of the outer and the inner zone. Knowing the relationship between viscosity and temperature behavior, an estimate of the inner zone average temperature (T_1) is possible. The methodology is still applicable in the presence of heterogeneities, provided a preliminary characterization of the permeability variations inside the test investigation distance is available. Therefore, a baseline HPT should be performed before any thermal injection. A comparative analysis of the test conducted during or after the injection campaign with the baseline test will allow a correct identification of the temperature front.

2.3. Design of Harmonic Pulse Testing for Thermal Front Monitoring

The fundamental oscillation period (T_f) of HPT needs to be selected to ensure an investigation distance (r_{max}) well into the undisturbed region ($r_{max} \gg r_1$). The fundamental injection period represents the maximum oscillation period in the Fourier analysis ($T_f = T_{max}$), thus it determines the test investigation distance (Salina Borello et al., 2019):

$$r_{max} = 1.5 \sqrt{\frac{k T_f}{2\pi \mu c_t \phi}} \qquad (14)$$

At the other side of the spectrum, the sampling resolution determines the lowest oscillation period component detectable on the pressure signal:

$$T_{min} = 2\Delta t \qquad (15)$$

Thus, the minimum distance investigated by the test, in ideal conditions (i.e. no noise) is:

$$r_{min} = 1.5 \sqrt{\frac{k \Delta t}{\pi \mu c_t \phi}} \qquad (16)$$

Eq. 16 may be used to calculate the sampling resolution necessary to characterize the near-wellbore heated zone. However, the harmonic components corresponding to the smaller oscillation periods can be affected by wellbore storage and skin phenomena limiting the detectability of the heated zone. The threshold oscillation period corresponding to the duration of wellbore storage effect can be evaluated by converting the time domain Chen & Bringham's criterion into the frequency domain:

$$T \leq \frac{50 C \mu}{kh} e^{0.14 S} \qquad (17)$$

Chen & Bringham's criterion is widely used to estimate the duration of the effects of wellbore storage in Pressure Transient Analysis (Chaudhry, 2004).

As a consequence of eq. 17, the heated zone can be characterized if:

$$T^* \gg \frac{50 C \mu}{kh} e^{0.14 S} \qquad (18)$$

where T* represents the critical oscillation period, i.e. the oscillation period of the harmonic component investigating the transition zone.

In dimensionless terms, defining the dimensionless period through $T_D = \frac{T}{2\pi} \frac{k}{\mu c_t \phi r_w^2}$ (Salina Borello et al., 2019), we have for the transition period (T_D^*), and the maximum (T_{Dmax}) and minimum periods (T_{Dmin}):

$$T_D^* = \frac{1}{4.5\pi} \left(\frac{r_1}{r_w} \right)^2 \gg \frac{50 C}{2\pi h c_t \phi r_w^2} e^{0.14 S} \qquad (19)$$

$$T_{Dmax} = \frac{T_f}{2\pi} \frac{k}{\mu c_t \phi r_w^2} \gg T_D^* \qquad (20)$$

$$T_{Dmin} = \frac{2\Delta t}{2\pi} \frac{k}{\mu c_t \phi r_w^2} \ll T_D^* \qquad (21)$$

Finally, test reliability strongly depends on the precision in the rate-change timing. In fact, errors in the rate-change timing (e_T) alter the harmonic component of frequency f ≥ 1/ e_T. Acceptable errors in timing should be properly evaluated case by case in the test design phase. In the case of thermal front monitoring the error should not mask the two horizontal stabilizations and the transition zone on the response derivative (|R'|):

$$e_T \ll T^* = \frac{\mu c_t \phi r_1^2}{2.25 k} \qquad (22)$$

The quality of the response function is less dependent on the magnitude of the two alternating rates and their precision (Salina Borello et al., 2017).

2.4. Geothermal Doublet

Two cases representative of a geothermal doublet system were considered (Table 1): after one month of water injection (case 1), and after six months of water injection (case 2). For each scenario, at the end of the injection period, a periodic test was performed at the injector (Table 2). The distance from the injector well to the producing well

Table 1

Simulation parameters for well, rock and water for the geothermal doublet scenario.

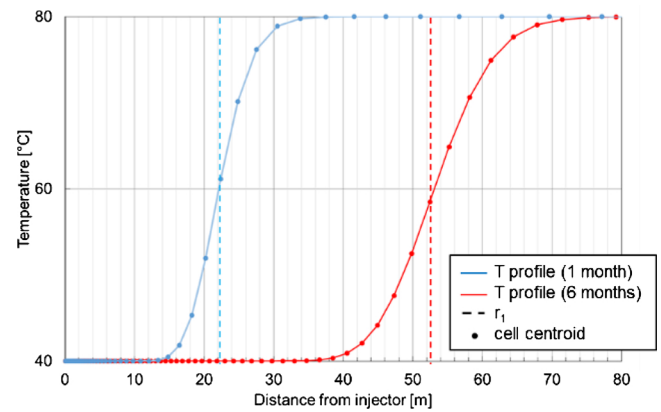| Aquifer data	
permeability (mD)	60
porosity (-)	0.2
reservoir temperature (°C)	80
pressure (bar)	200
depth (m ssl)	2000
net pay (m)	100
Well	
radius (m)	0.1
skin (-)	2
Rock	
compressibility (bar^{-1})	2.00E-05
thermal conductivity (W/K m)	2
heat capacity (J/kg K)	850
density (kg/m^3)	2600
Water	
compressibility (bar^{-1})	4.00E-05
thermal conductivity (W/K m)	0.6
heat capacity (J/kg K)	4148
salinity (ppm)	1000
density (kg/m^3)	1001
viscosity (mPa s) @ res temperature	0.34
viscosity (mPa s) @ inj temperature	0.66
injection temperature (°C)	40

Fig. 2. Numerically simulated thermal profiles: 1-month injection (light blue) vs 6 months of injection (red) and corresponding radial composite radii (dotted lines).

thermal front was mimicked with a fixed mobility ratio between the two zones; the heated zone extension and the mobility ratio were defined according to the results of the numerical simulation (Fig. 2); a sampling rate of 1 sec was imposed (Fig. 3). This gives the response of an ideal pressure profile not affected by noise that is used for validation purposes.

Finally, Gaussian noise was added to the simulated pressure data to mimic the response of a crystal quartz gauge characterized by an accuracy of ± 0.083 bar (Sclumberger, 2016) (Fig. 3), to verify the robustness of the interpretation methodology to noise.

2.5. Numerical Model of ATES

Heat storage cycles were simulated through a commercial 3D fluid-dynamic reservoir modeling tool taking into account the thermal phenomena. The synthetic aquifer model was based on a real formation, a possible candidate for ATES application in the Netherlands. Well, rock and water properties are reported in Table 3; annual heat storage cycle rate histories are reported in Table 4. The aquifer is characterized by 7 layers (numbered, in the following, from 1 to 7 starting from the top) of permeability ranging from 120 mD to 53797 mD. A sketch is provided in Fig. 4. Two layers are open to production/injection: number 3 and 5 from the top. They are characterized by permeability $k_h = 10760$ mD and $k_z = 2690$ mD and porosity $\varphi = 0.37$, separated by inter-layer 4 with porosity $\varphi = 0.5$ and permeability $k_h = 2391$ mD and $k_z = 24$ mD. Layer 2, at the top of the upper perforated layer has similar properties ($\varphi = 0.55$, $k_h = 2391$ mD, $k_z = 24$). Simulations of the whole domain with a grid refinement 10 m x 10 m x 10 m in the well area (Fig. 5) show that the upper perforated layer behaves as separated in terms of pressure response, due to the high permeability contrast. The temperature exchange between the upper perforated layer and the surrounding layers is also negligible compared to the exchange within the layer. For these reasons, a radial composite model should fit the interpretation of tests performed on such layer. We therefore focused on the upper layer only and simulated it as a single numerical layer of 1128 m x 1128 m areal extension and 30 m thickness. A significant grid refinement (cells of 4 m x 4 m) was imposed in an area of about
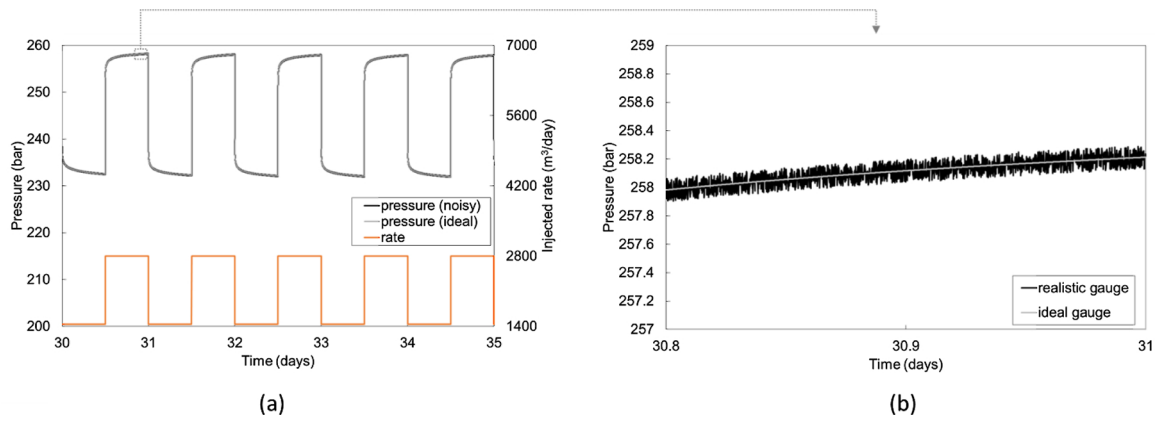
allowed the thermal front to develop with an axially symmetric shape, not altered by production at the producing well, thus representing a perfectly radial-composite scenario. We tested the reliability of our analytical radial-composite model (eq. 8 with the constants as defined in Appendix B) against a well-established analytical radial-composite model in the time domain (Olarewaju and Lee, 1989), implemented in a commercial software. A synthetic pressure response was generated in the time domain and interpreted with our model in the frequency domain. Furthermore, the impact of pressure gauge noise on the interpretation results was evaluated in a set of additional simulations. In the remainder of the paper we will refer to an ideal gauge when the simulated pressure response is not affected by noise and to a noisy or realistic gauge when the simulated pressure response is affected by gauge accuracy.

Synthetic data were generated by simulating the dynamic propagation of the temperature front with a single active well numerical simulator for fluid dynamics in porous media accounting for thermal effects (Verga et al., 2008, Verga et al., 2011, Verga et al., 2014). The resulting temperature profiles are shown in Fig. 2. The thermal front distance from the injector well, calculated as the distance at which the temperature reaches the average value between injection and reservoir temperature (60 °C in the considered validation cases) is 22 m for case 1 and 52 m for case 2 (Fig. 2).

In order to validate our solution against a well-established analytical solution, the pressure response to the pulse test was also simulated with a commercial analytical software in the time domain, where the

Table 2

Rate history of geothermal doublet scenarios.

Scenario	Test	Duration/period (days)	Rate (m^3/min)	Rate variation (m^3/min)	number of periods (-)
case 1	injection operations	30	2	-	-
	HPT1	1	1.5	± 0.5	5
case 2	injection operations	180	2	-	-
	HPT2	1	1.5	± 0.5	5

Fig. 3. Case 1: ideal pressure gauge (gray), generated with the analytical radial-composite model in the time domain (Olarewaju and Lee, 1989) and noisy pressure gauge (black) generated by adding Gaussian noise to the ideal gauge; (a) full 5-period duration, and (b) zoom.

Table 3
Simulation parameters for well, rock and water.

Well	
radius (m)	0.7874
skin (-)	0
Rock	
compressibility (bar^{-1})	2.18E-05
thermal conductivity (W/K m)	2.4
heat capacity (J/kg K)	850
density (kg/m^3)	2100
reservoir temperature (°C)	20
Water	
compressibility (bar^{-1})	4.00E-05
thermal conductivity (W/K m)	0.6
heat capacity (J/kg K)	4148
salinity (ppm)	20000
density (kg/m^3)	1016
viscosity (mPa s) @ res. temp.	1.13
viscosity (mPa s) @ inj. temp.	0.338
injection temperature (°C)	90

Table 4
Annual heat storage cycle.

	duration (days)	rate Well0 (m^3/day)	rate Well1 (m^3/day)
summer	90	− 3888	3888
autumn	60	0	0
winter	150	2328	− 2328
spring	60	0	0

900 m x 900 m containing the wells, with the double aim of correctly simulating the pressure gauge response and accurately describing the thermal front. Further away the grid size was increased to 20 m x 20 m and finally to 200 m x 200 m. The simulation grid is shown in Fig. 6. The gauge was supposed to be in the upper perforated layer, at 330 mssl. The initial pressure at datum was assumed hydrostatic (i.e., 33 bar); the initial temperature of the layer was 20 °C.

The same commercial software was used to simulate the HPTs pressure response, to verify the capability of the test in monitoring the heat front. The thermal front was monitored after the 5th summer of storage (4 complete storage cycles), after the subsequent winter, and again after the 15th summer of storage (14 complete storage cycles). Each test was conducted after a shut in period of one day. The data for the three HPTs in terms of test starting time, fundamental oscillation period (T_f), oscillating rates and number of oscillation periods are summarized in Table 5. Pressure and rate data are shown in Fig. 7. The HPT fundamental oscillation period (T_f) was set to 6 h (3 h of injection and 3 h of shut-in) to assure an investigation distance far enough to explore the undisturbed region (see eq. 14). Sampling resolution was set to $\Delta t = 1$ s to be able to characterize the heated zone properties (see eq. 16). Thus, in ideal conditions (i.e. no noise) with the applied setting we can explore the circular area between $r_{min} = 25$ m and $r_{max} = 2580$ m from Well1. In dimensionless terms (eq. 20–21), we have $70 < T_D < 7.6e5$. Preliminary synthetic tests confirmed that the first horizontal stabilization was hardly detectable with $\Delta t > 1$ s.

3. Results

3.1. Test on Geothermal Doublet

Our model was initially validated against a conventional analytical radial composite model adopted for the Geothermal doublet, assuming step-change temperature profiles. For the ideal gauge, the
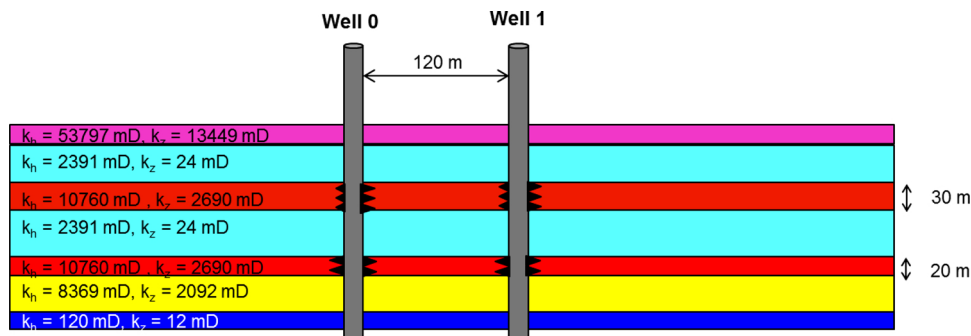

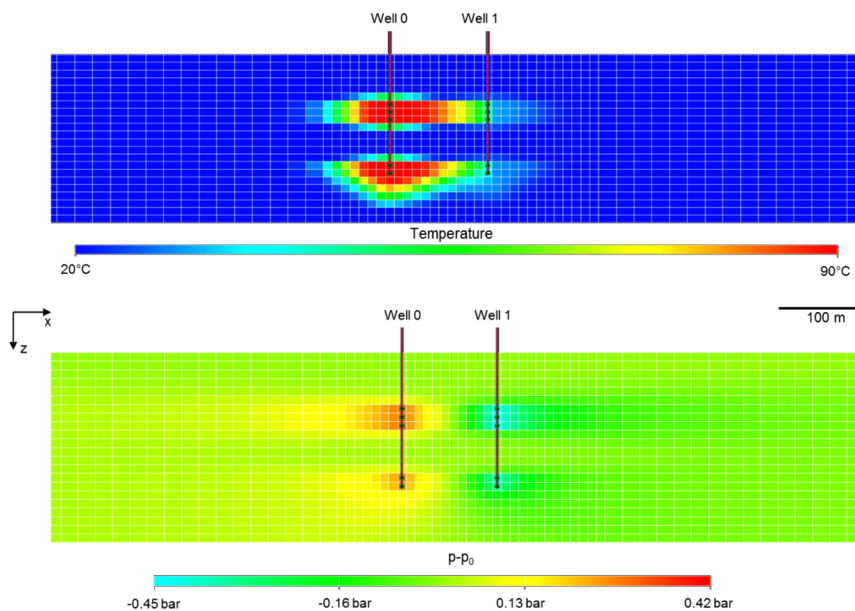**Fig. 4.** Sketch of aquifer layers (x-z cross section).

Fig. 5. Preliminary simulation results after the 5th summer of injection (zoom of x-z cross section). Grid refinement 10 m x 10 m x10 m.
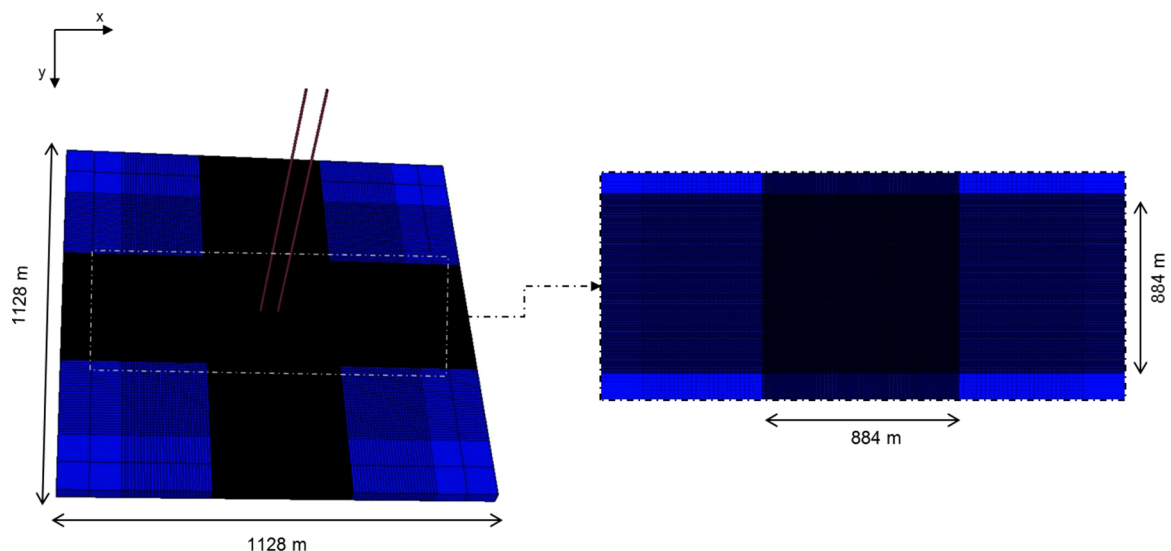

Fig. 6. Grid for final simulations (top view and zoom).

dimensionless log-log plot in the frequency domain (representing $|R_D|$ and $|R_D'|$ as defined in paragraph 2.2) and the analytical interpretation model are shown in Fig. 8a. Case 1 is depicted in blue, while case 2 is depicted in red. In both cases, the model provides a good match of the data and a correct value of the inner thermal zone radius. Analysis of the phase shift ($\angle R$) confirms the interpretation (Fig. 9a). The same behavior (Fig. 10) is observed when considering pressure data generated with the numerically simulated temperature profiles (Fig. 2): except for the very beginning of the transition zone, the amplitude and phase behavior is very similar to the one of the step-change profile assumption. The noisy-gauge analysis is shown in Fig. 8b and Fig. 9b. In

both cases the inner radius is still detectable. In fact, the noise mostly affects the first stabilization, while the transition zone and the second stabilization can be clearly detected (Fig. 8b); a similar influence is observed on phase shift (Fig. 9b). Therefore, HPT interpretation provides a reliable monitoring of the thermal front evolution.

The complete injection history is known in these synthetic cases and the pressures are not affected by interference phenomena. Therefore, conventional Pressure Transient Analysis (PTA) in time domain (Bourdet et al, 1984) can also be applied. The corresponding log-log plot for a single injection period is shown for both the ideal gauge (Fig. 11a) and the noisy gauge (Fig. 11b) in dimensionless terms

Table 5
HPT tests for heat front monitoring on Well 0.

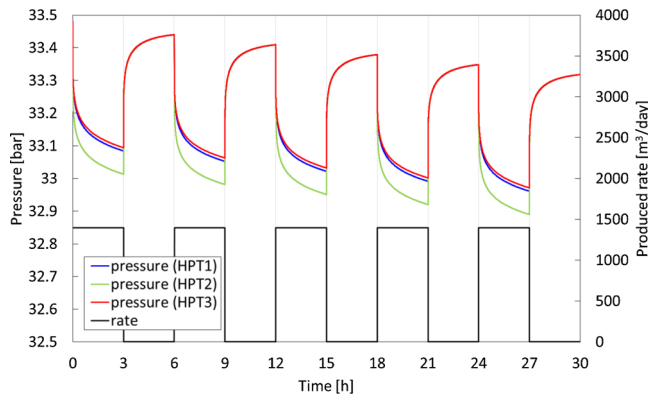| HPT Test	HPT starting time	T_f (h)	Rate 1 (m3/day)	Rate 2 (m3/day)	Number of periods (-)
HPT1	after 5th summer	6	1396.8	0	5
HPT2	after 5th winter	6	1396.8	0	5
HPT3	after 15th summer	6	1396.8	0	5

Fig. 7. Simulated pressure data (red, blue, and green curve, left axis) from harmonic pumping tests 1 to 3 (see Table 5) at tested well (Well0) with the flow-rate protocol given by the black curve (right axis).

(Bourdet, 2002). Based on that, results obtained in time and frequency domains can be directly compared (Fig. 8a vs Fig. 11a for the ideal gauge; Fig. 8b and Fig. 11b for the noisy gauge) and superposed on the same log-log plot (Salina Borello et al. 2019). Comparison of Fig. 8b and Fig. 11b shows the different impact of noise in time domain (PTA) and frequency domain (HPT). Conventional PTA is mainly affected by noise in the part of the curve, corresponding to the formation volume containing the thermal front (middle-time in PTA terminology). HPT is affected by noise in the part of the curve, representing the high-frequency components (smaller T) which investigate the near wellbore area (early-time in PTA terminology). As a consequence, the thermal front evolution can be more easily detected through HPT interpretation in the frequency domain. Furthermore, a combined analysis, obtained superposing PTA and HPT curves in dimensionless terms, can improve interpretation reliability minimizing uncertainties. The combined analysis follows three steps: (1) superposed representation of PTA and HPT curves in dimensionless terms (Fig. 12a); (2) application of a low-pass filter to both time data and frequency data to obtain a single clean derivative plot (Fig. 12b); (3) interpretation of the obtained derivative plot with the presented frequency model.

3.2. Application to ATES

In the after-summer scenario of the 5th storage cycle (Fig. 13a), the simulated temperature changes gradually, but not linearly, from the injection temperature (90 °C) to the temperature value in the proximity of the front (about 60 °C), beyond which an abrupt change towards the

initial aquifer temperature (20 °C) is observed. Due to the simultaneous production in Well1, the heated zone is off-centered with respect to Well 0; it elongates toward producing Well 1, thus assuming an almost oval shape. Temperature distribution on the cross section along the line connecting the two wells is provided in Fig. 14.

After seven months, in the after winter scenario (Fig. 13b), the situation is significantly different. The temperature around Well 0 has decreased to 50-70 °C (Fig. 14) and the heated zone extension has decreased, too. Pushed by the cold-water injection at Well 1, the thermal front position along the intra-well direction moves towards Well 0 and the shape of heated zone becomes irregular. With the progression of seasonal cycles, the after-summer heated zones tend to expand, becoming rounder (Fig. 13c).

For all tests (Fig. 15), the second stabilization allowed for correct identification of a permeability value of about 11D and a zero skin value. Comparing after-summer and after-winter derivatives (Fig. 15a), a significantly different first stabilization is observable, which corresponds to a different near-wellbore viscosity and therefore a different temperature. The extent of the near-wellbore heated zone indicated by the after-summer derivative is also significantly larger than the extent indicated by the after-winter derivative. When comparing the derivatives of tests conducted after-summer of the 5th and of the 15th storage cycle (Fig. 15c), the level of the first stabilization is practically the same, indicating similar temperature, but a difference is observed for the extent of the heated zone. The size is slightly larger after the summer of the 15th cycle. Phase shift analysis (Fig. 15b and Fig. 15c) confirms the interpretation from the modulus of the derivative of the response and allows a better calibration of the heated zone extension, showing a good sensitivity even to small heat zone changes, as in HPT1 vs HPT3 ($\Delta r_1 = 10\%$). This is in accordance with Cheng & Renner (2018), who documented that phase shift is a particularly sensitive tool for concentric-shell models.

We already indicated that the simultaneous injection and production in the two wells causes a distortion from axial symmetry. The heated zone is neither centered around Well 0, nor circular (Fig. 13). To facilitate a quantitative comparison between the numerical solution and the radial composite model, we calculated an equivalent radius of the heated zone from the temperature map. First, we calculate a threshold temperature ($T_{threshold}$) as the average between the temperature at the wellbore and far into the reservoir, yielding $T_{threshold} = 55\,°C$ in the after-summer scenario and $T_{threshold} = 45\,°C$ in the after-winter scenario. Then we applied $T_{threshold}$ as a temperature filter to identify the heated zone and we calculated the median temperature values (T_m) of the selected cells. We approximated the heated zone with an equivalent circumference, i.e. the circumference with radius $r_{eq} = \sqrt{\frac{A}{\pi}}$, that have an
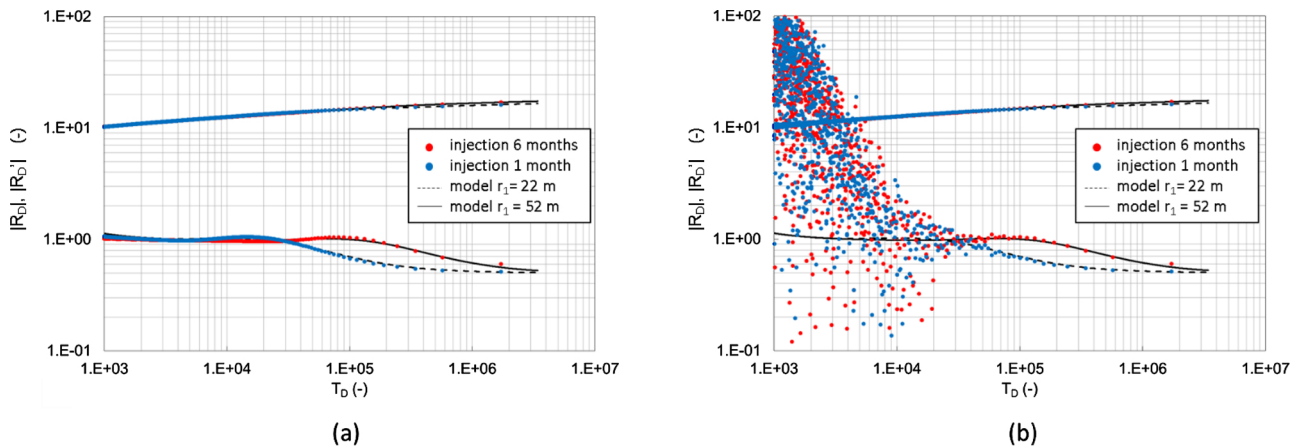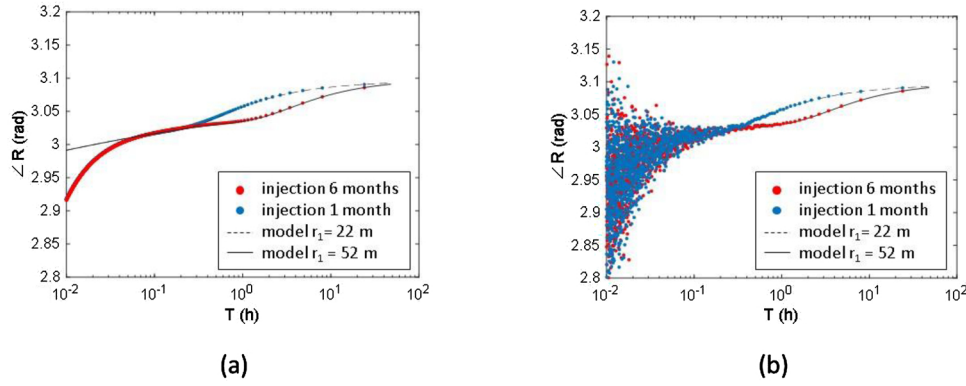

Fig. 8. Comparison of reservoir response after 1 month of injection (blue) vs. after 6 months of injection (red): frequency analysis of the ideal gauge (a) and of the noisy gauge (b), reported in amplitude of dimensionless response ($|R_D|$) and amplitude of dimensionless response derivative ($|R_D'|$) vs. dimensionless oscillation period (T_D); data generated with the analytical radial-composite model in the time domain (Olarewaju and Lee, 1989).

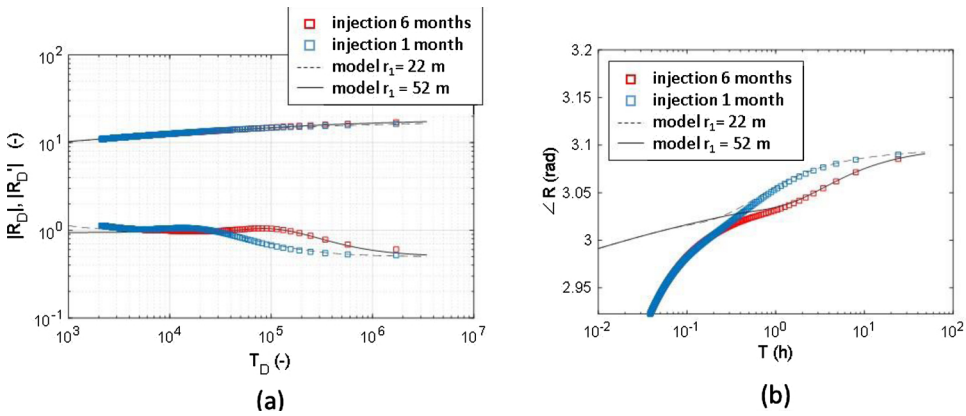**Fig. 9.** Comparison of reservoir response after 1 month of injection (blue) vs. after 6 months of injection (red): frequency analysis of the ideal gauge (a) and of the noisy gauge (b), in terms of phase shift ($\angle R$) vs. oscillation period (T); data generated with the analytical radial-composite model in the time domain (Olarewaju and Lee, 1989).

Fig. 10. Comparison of the reservoir response in the active well (pulser) after 1 month of injection (blue) vs. after 6 months of injection (red): frequency analysis of the response amplitude ($|R|$) and amplitude derivative ($|R'|$) (a) and phase shift ($\angle R$) (b); data generated with the numerical simulator accounting for thermal effects.

area equivalent to the heated zone (see Fig. 16). The obtained approximation of the heated zone are also reported in Table 6. A good agreement was observed in all scenarios both in terms of median temperature (T_m), which differs from the estimated temperature (T_1) by less than 4 °C, and in terms of heated equivalent radius (r_{eq}), which differs from the interpreted r_1 less than 10%. We conclude that the approximation with a circular heated zone and a step function for the temperature fits the synthetic data, and that the numbers derived for heated area and temperature change close to the injector characterize the actual system well.

4. Discussion

To correctly design and perform an HPT test for heat-zone monitoring in an ATES system, some issues must be considered. To assure test interpretability, the first and the second horizontal stabilizations, representative of the heated zone and the undisturbed zone, respectively, must be clearly detectable on the log-log plot of the response derivative (see section 2.2). Thus, a proper test design is necessary (section 2.3). In the first place, such a design includes a duration of the fundamental oscillation period (i.e. the sum of the durations of the two alternating constant rates) that is long enough to investigate the undisturbed zone (eq. 14). In the presented ATES case, in which the permeability is extremely high (about 11 D), an oscillation period $T_f \geq$ 6 h is sufficient to capture the stabilization corresponding to undisturbed conditions (Fig. 15). Considering that 5 oscillations are required (Salina Borello et al., 2017), the total test duration is 30 h, which is compatible with the storage operations. On the one hand, high
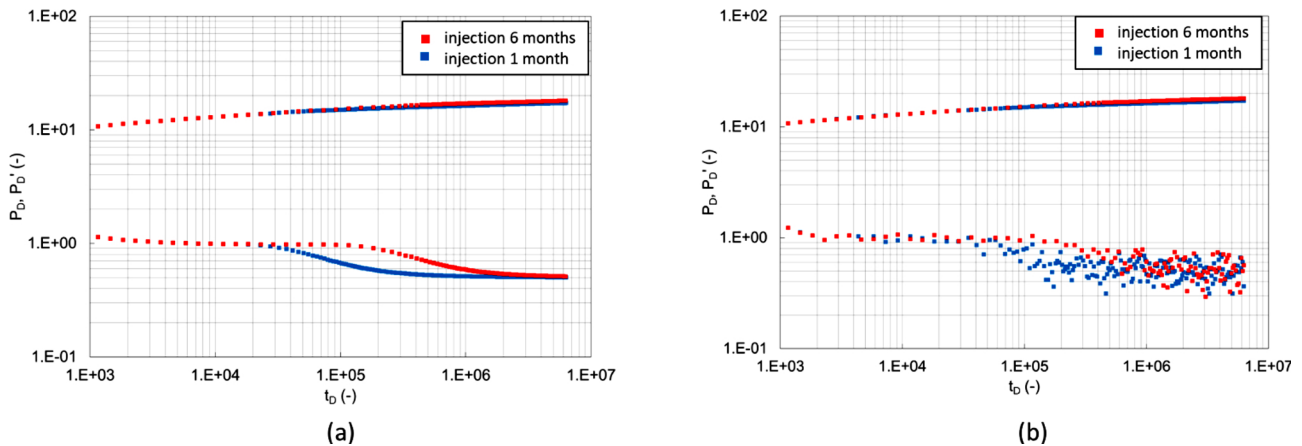

Fig. 11. Comparison of reservoir response after 1 month of injection (blue) vs. after 6 months of injection (red): conventional Pressure Transient Analysis of the ideal gauge (a) vs. the noisy gauge (b), reported in dimensionless pressure (P_D) and dimensionless pressure derivative (P_D') vs. dimensionless time (t_D); data generated with the analytical radial-composite model in the time domain (Olarewaju and Lee, 1989).
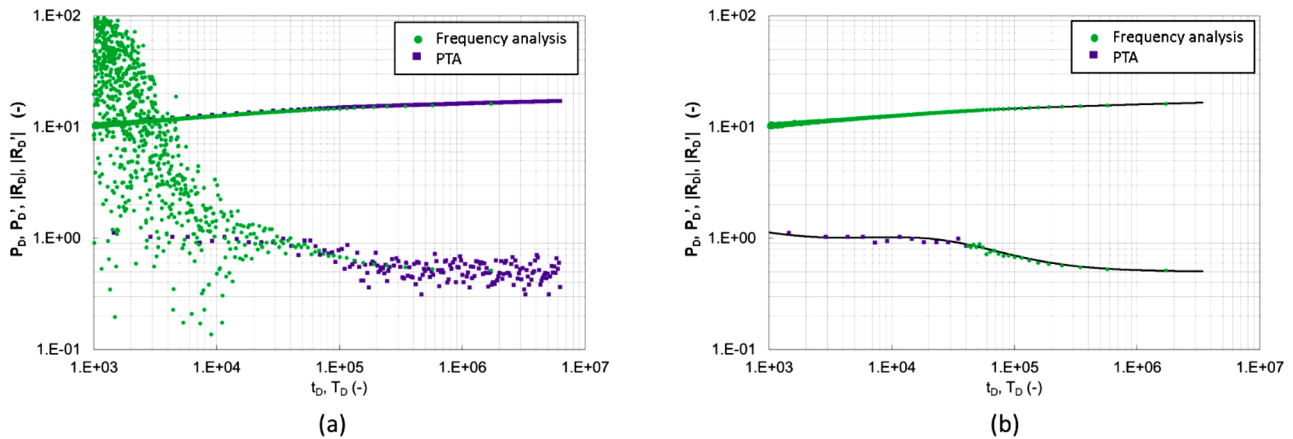
Fig. 12. Maximization of information extraction from the noisy gauge by combining the analysis of time and frequency data in dimensionless terms (case1): (a) superposition of time and frequency analysis in dimensionless term; (b) application of low-pass filter to both time data and frequency data to obtain a single clean derivative plot; data generated with the analytical radial-composite model in the time domain (Olarewaju and Lee, 1989).

permeability allows reducing test duration; on the other hand, it implies the need of high precision in the test execution (eq. 22) and a high pressure sampling rate (eq. 16). In fact, the first stabilization, representative of the heated zone, is investigated by high frequency components. As an example, in the presented ATES case, the first horizontal stabilization covers oscillation periods in the range 0.003-0.03 h (from 10 s to less than 2 min). At the same time, these fast oscillation responses are impacted most by the wellbore storage. Thus, to be able to capture the first stabilization, the HPT test data must have: 1) a pressure sampling rate significantly below this range (i.e. $\Delta t < < 10\,s$); 2) rate changes performed fast enough in order to also be within this range (i.e. $e_T \leq 10\,s$). Still, the wellbore storage effect may pose a lower limit to the observable radii of thermal fronts. In case of high-

permeability formations, as in the considered ATES example, gauge accuracy can have a significant impact on detectability of the first stabilization. However, a combined analysis in both frequency and time domain, when feasible, can significantly enhance interpretation reliability.

Data interpretability of a noisy response spectrum could also be improved by the joint interpretation of a sequence of two or more HPTs characterized by different fundamental oscillation periods and therefore focusing on different investigated areas. In fact, as already discussed by the authors (Salina Borello et al., 2019), the area investigated by the test is directly proportional to the square root of the fundamental oscillation period T_f (eq. 14). Moreover, the harmonic components are odd fractions of fundamental oscillation period (T_f, $T_f/3$, $T_f/5$, $T_f/7$, …).
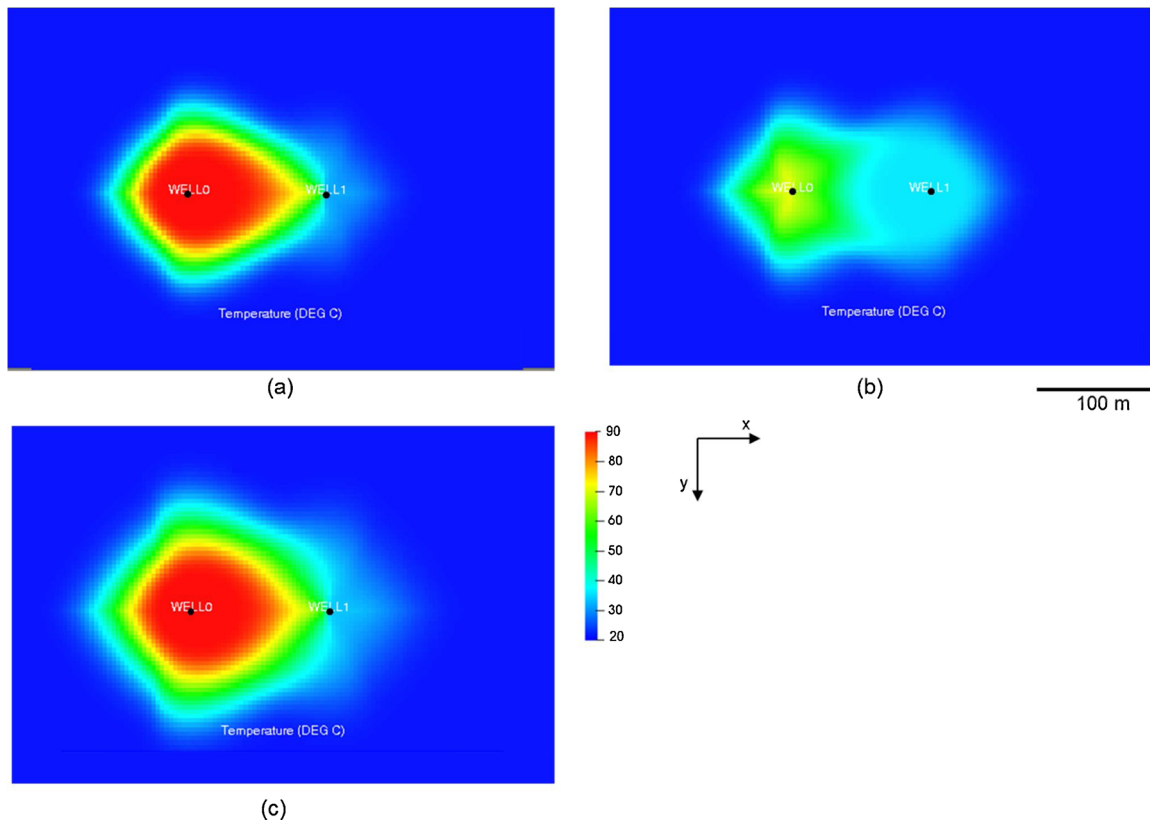

Fig. 13. Simulation results: comparison between temperature profiles (a) after summer of the 5th storage cycle, (b) after winter of the 5th storage cycle and (c) after summer of the 15th storage cycle; zoom of top views.
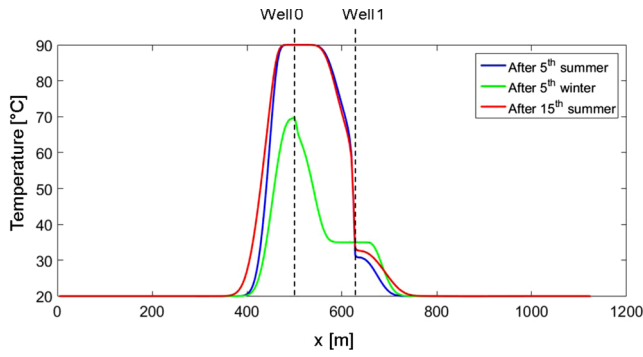
Fig. 14. Temperature distributions along the x-directrix crossing the two wells. The pressure trends of the simulated HPTs were analyzed in the frequency domain as described in section 2.2. Log-log plots of the moduli of R and R' versus oscillation period ($2\pi/\omega$) and semilog plots of the phase of R versus oscillation period are shown in Fig. 15. Data were interpreted with our radial composite model in the frequency domain (eq. 8) to give an estimate of the extension of inner zone radius (r_1) and of the mobility ratio between inner and outer zone (M), leading to an estimate of the inner zone average temperature (T_1) (Table 6).

As a consequence, in the frequency analysis the density of points in a range of T values corresponding to a horizontal stabilization depends on T_f. Moreover, along with noise on recorded pressure due to gauge accuracy, imprecision on rate changes (delay and/ or advance) is responsible of noise on the response spectrum as well. Our experience on real cases (Salina Borello et al. 2017, Salina Borello et al. 2019) shows that irregularities on rate changes are often higher for tests
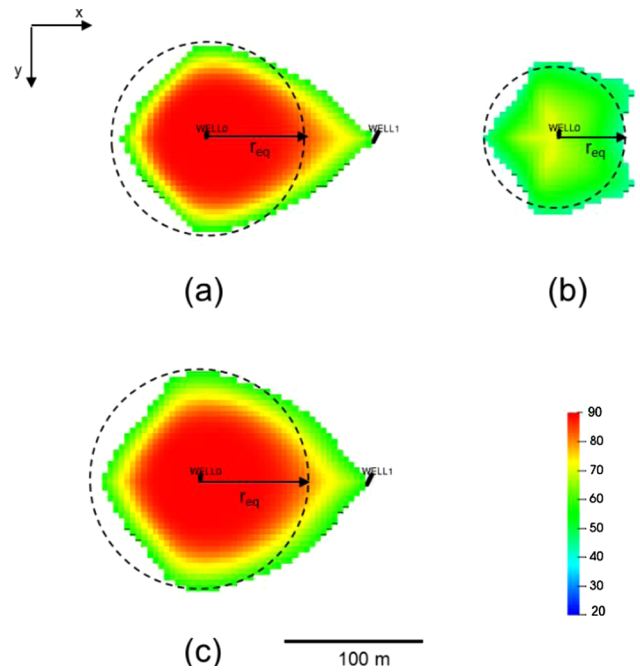

Fig. 16. Approximation of the heated zone with the equivalent circumference centered in Well 0 (a) after 5th summer, (b) after 5th winter and (c) after 15th summer.
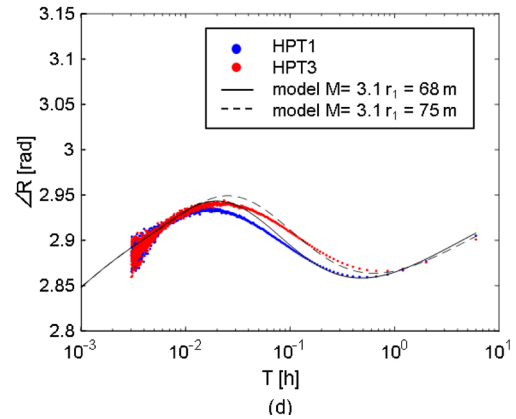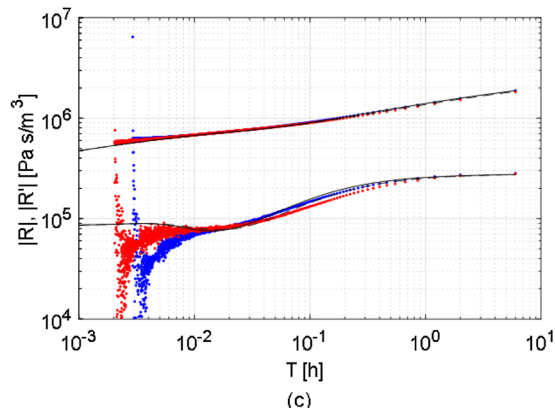

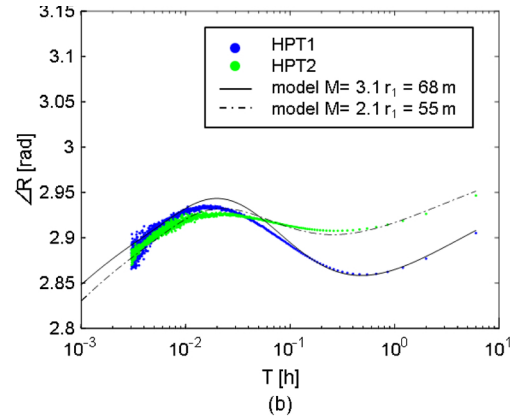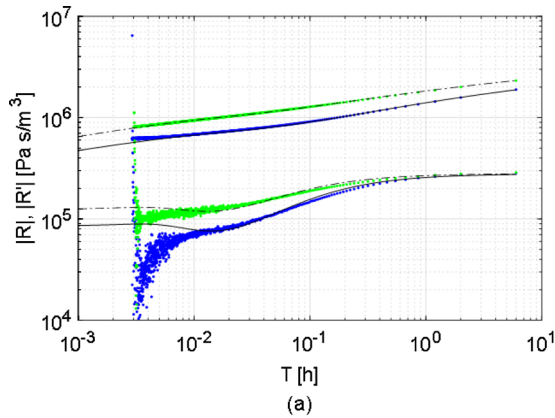**Fig. 15.** HPT results: comparison between reservoir response after summer (blue) vs. after winter (green) of the 5th storage cycle in terms of (a) amplitude ($|R|$) and amplitude derivative ($|R'|$) and (b) phase shift ($\angle R$); comparison between reservoir response after summer of the 5th storage cycle (blue) vs. 15th storage cycle (red) in terms of (c) amplitude and amplitude derivative and (d) phase shift.

Table 6
Tests interpretation results with radial composite model in the frequency domain compared with the approximation of the simulated heated zone to an equivalent circumference centered in Well 0.

HPT Starting time	Radial composite HPT interpretation			Numerical simulation		
	$M = \mu_2/\mu_1$	T_1 (°C)	r_1 (m)	heated zone (°C)	T_m (°C)	r_{eq} (m)
after 5th summer	3.1	84	68	55°-90 °C	83.4 °C	69.8
after 5th winter	2.1	58	55	45°-70 °C	55.9 C°	50.9
after 15th summer	3.1	84	75	55°-90 °C	80 °C	78.9

characterized by a longer T_f, which implies that usually only the first 10-20 harmonic component (T_f, $T_f/3$, $T_f/5$, etc) are undisturbed. Analogously to eq. 14, the lower limit of the investigation area covered by N interpretable components is directly proportional to the square root of $T_f/(2N-1)$. Thus, two subsequent HPTs can be designed to better focus the investigations separately on the inner zone and on the outer zone.

When the test is well designed, changes of the heated zone within the storage cycle (i.e. between after-summer and after-winter) as well as gradual changes over the years are detectable on the log-log plot from the variations in value and position of the first horizontal stabilization observable on the response derivative (Fig. 15). Clearly, the higher the viscosity contrast, the easier the detection on the log-log plot, due to the larger difference between the horizontal stabilization levels for the two zones. However, relatively small values of the viscosity contrast already allow the application of our methodology. Only values near to M = 1, such as.$0.75 < M < 1.25$, could be critical. Similar criticalities arise if the heated zone extension is very limited. Harmonic Pulse Testing is thus suitable for heated-zone monitoring in a wide range of viscosity contrasts.

The radially symmetric model in the test interpretation may not exactly correspond to reality, where the shape of the heated zone may be non-symmetric because of the second well in the ATES doublet system (Well 1, in Fig. 13) or because of other heterogeneities. As a consequence, the prediction of the thermal front position between the two wells is subject to uncertainty. In addition, the actual heat front is gradual rather than a step function, therefore part of the injected heat is advancing the modeled front. However, the test interpretation gives valuable information about changes in average heated zone extension and temperature (Table 6).

5. Conclusions

In this paper, we have expanded our earlier work on Harmonic Pulse Testing (HPT) to incorporate the effect of a temperature front moving into the reservoir due to injection of hot (or cold) water. The goal was to be able to employ HPT for monitoring the heat front with particular focus to Aquifer Thermal Energy Storage (ATES). Reliable monitoring requires a baseline HPT test, before injection, to assess the possible presence of heterogeneities. Tests after the summer injection campaign and after the winter production campaign can then be employed over the years.

The HPT interpretation with the presented radial composite model solution was preliminarily applied to monitor the thermal front evolution in a synthetic doublet system showing axial symmetry and thus validated against an analytical model. The methodology provided reliable estimates of thermal zone extension and average temperature around the injector for an ideal pressure gauge, not affected by noise, and a realistic gauge, affected by noise.

Furthermore, we demonstrated that HPT can be applied to monitor

the thermal front of a synthetic Aquifer Thermal Energy Storage (ATES) if a proper test design is applied:

- duration of the fundamental oscillation period is long enough to investigate the undisturbed zone;
- rate changes are sufficiently precise, i.e. maximum acceptable advance/delays are significantly lower than the oscillation period corresponding to the thermal front expected position;
- gauge pressure sampling is close enough to investigate the heated zone.

Agreement was observed in all scenarios both in terms of median temperature (T_m), which differed from the estimated temperature (T_1) less than 4 °C, and in terms of heated equivalent radius (r_{eq}), which differed from the interpreted r_1 less than 10%.

The information obtained from the HPT interpretation does not exactly reproduce the shape of the heated zone of the ATES doublet system, which is not a step function in temperature and is not exactly axially symmetric around the tested well. The latter is due to the contemporary injection/production in the second well or to other heterogeneities in the reservoir. As a consequence, HPT interpretation with the radial composite model may not correctly predict the front position in between the two wells. However, the test interpretation gives valuable information on the extent of the heated zone and its temperature. Moreover, a planning of systematic HPT allows for monitoring variations of the heated zone during the storage cycle and over the years, thus enabling adjustment and fine tuning of the field operations.

Data Availability

Datasets related to this article can be found at https://doi.org/10.17632/ddzcwy53vr.1, an open-source online data repository hosted at Mendeley Data (Chen and Maloof, 2017).

CRediT authorship contribution statement

Peter A. Fokker: Conceptualization, Methodology, Software, Writing - original draft, Writing - review & editing. **Eloisa Salina Borello:** Methodology, Software, Data curation, Validation, Visualization, Writing - original draft, Writing - review & editing. **Dario Viberti:** Conceptualization, Validation, Writing - original draft, Writing - review & editing, Supervision. **Francesca Verga:** Project administration, Resources, Conceptualization. **Jan-Diederik van Wees:** Conceptualization, Resources.

Declaration of Competing Interest

The authors report no declarations of interest.

Appendix A

In the following we incorporate skin in the well pressure expression and we derive the general system response in a radial composite scenario of radius r_1.

The pressure in the well is different from the pressure at the well location in the reservoir, because of skin. Skin is introduced as an instantaneous pressure drop due to, e.g., a mudcake or wellbore impairment as at term proportional to the flow rate:

$$p_{well} = p_{res}(r_w) + \frac{1}{2\pi h \lambda_1} q_{perfs} S \tag{23}$$

where $\lambda_i = \frac{k_i}{\mu_i}$ is the mobility and h is the reservoir thickness. The rate is taken positive for injection.

Rate is related to pressure gradient throw Darcy law. At the well sandface ($r = r_w$), considering eq. 3 we have:

$$q_{perfs} = -2\pi h \lambda_1 \left[r \frac{\partial p}{\partial r} \right]_{r=r_w} = -2\pi h \lambda_1 \left[r \frac{dg_\omega}{dr} \right]_{r=r_w} e^{i\omega t} \tag{24}$$

From eq. (7), applying the differential properties of Bessel functions (Abramowitz and Stegun, 1964) we obtain:

$$\frac{dg_\omega}{dr}(r) = -\zeta q_\omega C_K K_1(\zeta r) + \zeta q_\omega C_I I_1(\zeta r) \tag{25}$$

From eq. (3), eq. (7) and eq.(23–25), the response function, in the pulser well is:

$$R_\omega^{pulser} = \frac{p_{well}}{q_{well}} = \frac{1}{q_\omega e^{i\omega t}} \{p_{res}(r_w) + \frac{1}{2\pi h \lambda_1} q_{perfs} S\} = \frac{g_\omega(r_w)}{q_\omega} - \frac{1}{q_\omega} S [r \frac{dg_\omega}{dr}]_{r=r_w} = C_K^1 K_0(\zeta_1 r_w) + C_I^1 I_0(\zeta_1 r_w) + S \zeta_1 r_w [C_K^1 K_1(\zeta_1 r_w) - C_I^1 I_1(\zeta_1 r_w)] \tag{26}$$

If we monitor an observation well, we directly see the reservoir pressure at that location. From eq. (3) and eq. (7) if the observation well is inside (zone 1) or outside (zone 2) the area near wellbore with altered temperature, we respectively have:

$$R_\omega^{obs} = \frac{p_{well}}{q_{well}} = \frac{g_\omega(r_{obs})}{q_\omega} = \begin{cases} C_K^1 K_0(\zeta_1 r_{obs}) + C_I^1 I_0(\zeta_1 r_{obs}) & (r_{obs} < r_1) \\ C_K^2 K_0(\zeta_2 r_{obs}) + C_I^2 I_0(\zeta_2 r_{obs}) & (r_{obs} \geq r_1) \end{cases} \tag{27}$$

where parameters $C_K^1, C_I^1, C_K^2, C_I^2$ have to be determined through imposing boundary conditions and continuity at the interface. Details follow in Appendix B.

Appendix B

This Appendix provides the details on the determination of the free parameters $C_K^1, C_I^1, C_K^2, C_I^2$ in the solution for the harmonic response in a pulse test in a radial composite system with two zones (eq. 26 and eq. 27). The two zones have different mobility due to the different viscosity resulting from the temperatures in the two zones. Coefficients $C_K^1, C_I^1, C_K^2, C_I^2$ have to be determined through imposing the following conditions: (1) reservoir inflow from the wellbore; (2) continuity of pressure at the interface; (3) continuity of flow at the interface; and (4) vanishing pressure disturbance at infinity.

We start with the inflow condition from the wellbore (condition 1). Because the wellbore has a nonzero volume (V_{well}) and the injected fluid has a nonzero compressibility (c), part of the injected fluid is "stored" in the wellbore when the pressure is changing. The resulting rate sandface is thus:

$$q_{perfs} = q_{well} - C \frac{dp_{well}}{dt} \tag{28}$$

where, $C = cV_{well}$ is the wellbore storage coefficient.

Substitution of eq. 3 and eq. 23 in eq. 28 yields:

$$q_{perfs} = q_\omega e^{i\omega t} - C \frac{d}{dt}(p_{res}(r_w) + \frac{1}{2\pi h \lambda_1} q_{perfs} S) \tag{29}$$

The time dependence of rate (eq. 3) and pressure (eq. 4) is fully contained in the factor $e^{i\omega t}$, therefore $\frac{d}{dt}[p(r_w, t)] = \frac{d}{dt}[g(r_w)e^{i\omega t}] = i\omega g(r_w)e^{i\omega t} = i\omega p(r_w, t)$, and similarly $\frac{d}{dt}[q_{perfs}] = i\omega q_{perfs}$. Eq. 29 thus yields:

$$q_{perfs} = q_\omega e^{i\omega t} - C i\omega (p_{res}(r_w) + \frac{1}{2\pi h \lambda_1} q_{perfs} S) \tag{30}$$

Substitution of the Darcy expression for the rate at the sandface (eq.11) in eq. 30 gives:

$$-2\pi h \lambda_1 [r \frac{dg_\omega}{dr}]_{r=r_w} = q_\omega - i\omega C(g_\omega(r_\omega) - [r \frac{dg_\omega}{dr}]_{r=r_w} S) \tag{31}$$

Substituting eq. 7 in eq. 31 and grouping for C_K^1 and C_I^1 gives:

$$C_K^1 [2\pi h \zeta_1 r_w \lambda_1 K_1(\zeta_1 r_w) + i\omega C K_0(\zeta_1 r_w) + i\omega C S r_w \zeta_1 K_1(\zeta_1 r_w)] + C_I^1 [-2\pi h \zeta_1 r_w \lambda_1 I_1(\zeta_1 r_w) + i\omega C I_0(\zeta_1 r_w) - i\omega C S r_w \zeta_1 I_1(\zeta_1 r_w)] = 1 \tag{32}$$

This equation poses the first equation for the determination of the parameters in the solution (Eq. 7).

At the fluid front ($r = r_1$) between the inner zone, characterized by mobility λ_1, diffusion η_1, ζ_1, and coefficients C_K^1, C_I^1, and the outer zone, characterized by mobility λ_2, diffusion η_2, ζ_2, and coefficients C_K^2, C_I^2, continuity of pressure (condition 2) and flow rate (condition 3) must be guaranteed.

According to eq. 4 and 7, pressure of the ith zone writes:

$$(C_K^i K_0(\zeta_i r) + C_I^i I_0(\zeta_i r))e^{i\omega t} \tag{33}$$

Imposing continuity of pressure (condition 2) at $r = r_1$, yields:

$$C_K^1 K_0(\zeta_1 r_1) + C_I^1 I_0(\zeta_1 r_1) = C_K^2 K_0(\zeta_2 r_1) + C_I^2 I_0(\zeta_2 r_1) \tag{34}$$

According to Darcy law and eq. 25, flow rate of the ith zone writes:

$$- 2\pi r h \lambda_i \left[\frac{dg_\omega}{dr} \right] e^{i\omega t} = -2\pi h e^{i\omega t} q_\omega \lambda_i \zeta_i r \left[-C_K^i K_1(\zeta_i r) + C_I^i I_1(\zeta_i r) \right]$$

(35)

Imposing continuity of flow rate (condition 3) at $r = r_1$, yields:

$$- \lambda_1 \zeta_1 r_1 C_K^1 K_1(\zeta_1 r_1) + \lambda_1 \zeta_1 r_1 C_I^1 I_1(\zeta_1 r_1) = -\lambda_2 \zeta_2 r_1 C_K^2 K_1(\zeta_2 r_1) + \lambda_2 \zeta_2 r_1 C_I^2 I_1(\zeta_2 r_1)$$

(36)

Finally, vanishing pressures in infinity (condition 4) requires $[g_\omega]_{r\to\infty} = 0$. Writing eq. (7) for the outer zone and remembering that for $r \to \infty$ Bessel functions K vanishes while Bessel functions I go to infinity, condition 4 yields:

$$C_I^2 = 0$$

(37)

Substituting eq. 37 in eq. 36 and eq. 34 and putting together with eq. 33 we obtain a linear set of equations for the three remaining unknowns as follows:

$$\begin{pmatrix} i\omega C k_{001} + (2\pi h \lambda_1 + i\omega CS)k_{101} & i\omega C i_{001} - (2\pi h \lambda_1 + i\omega CS)i_{101} & 0 \\ k_{011} & i_{011} & -k_{012} \\ -\lambda_1 k_{111} & \lambda_1 i_{111} & \lambda_2 k_{112} \end{pmatrix} \begin{pmatrix} C_K^1 \\ C_I^1 \\ C_K^2 \end{pmatrix} = \begin{pmatrix} 1 \\ 0 \\ 0 \end{pmatrix}$$

(38)

where

$$
\begin{aligned}
k_{001} &= K_0(\zeta_1 r_w) & k_{101} &= K_1(\zeta_1 r_w)\zeta_1 r_w \\
i_{001} &= I_0(\zeta_1 r_w) & i_{101} &= I_1(\zeta_1 r_w)\zeta_1 r_w \\
k_{011} &= K_0(\zeta_1 r_1) & k_{111} &= K_1(\zeta_1 r_1)\zeta_1 r_1 \\
i_{011} &= I_0(\zeta_1 r_1) & i_{111} &= I_1(\zeta_1 r_1)\zeta_1 r_1 \\
k_{012} &= K_0(\zeta_2 r_1) & k_{112} &= K_1(\zeta_2 r_1)\zeta_2 r_1
\end{aligned}
$$

(39)

The solution to this set of equations is easily obtainable by matrix inversion; the parameters C_K^1, C_I^1, C_K^2 will depend on skin (S), wellbore storage coefficient (C), position of the temperature interface (r_1), mobility (λ_1, λ_2) and diffusion coefficient (η_1, η_2) in the two zones and the angular frequency (ω).

Appendix C. Supplementary data

Supplementary material related to this article can be found, in the online version, at doi:https://doi.org/10.1016/j.geothermics.2020.101942.

References

Abramowitz, M., Stegun, I., 1964. Handbook of Mathematical Functions. Chap. 9. Dover Publications, New York.

Ahn, S., Horne, R.N., 2010. Estimating permeability distributions from pressure pulse testing. In: Proceedings - SPE Annual Technical Conference and Exhibition, 3:2388–2403. Florence. https://doi.org/10.2118/134391-MS.

Black, J.H., Kipp, K.L.J., 1981. Determination of hydrogeological parameters using sinusoidal pressure tests: A theoretical appraisal. Water Resources Research 17 (3), 686–692. https://doi.org/10.1029/WR017i003p00686.

Bourdet, D., 2002. Well west analysis: The Use of Advanced Interpretation Models: Handbook of Petroleum Exploration and Production 3 Elsevier Science B.V., Amsterdam ISBN: 978-0-444-54988-4.

Bourdet, D., Whittle, T.M., Douglas, A.A., Pirard, Y.M., 1983. New set of type curves simplifies well test analysis. World Oil 196 (6), 95–106.

Cardiff, M., Bakhos, T., Kitanidis, P.K., Barrash, W., 2013. Aquifer heterogeneity characterization with oscillatory pumping: Sensitivity analysis and imaging potential. Water Resources Research 49, 5395–5410. https://doi.org/10.1002/wrcr.20356.

Cardiff, M., Barrash, W., 2015. Analytical and semi-analytical tools for the design of oscillatory pumping tests. Groundwater 53 (6), 896–907. https://doi.org/10.1111/gwat.12308.

Cardiff, M., Zhou, Y., Barrash, W., Kitanidis, P.K., 2019. Aquifer Imaging with Oscillatory Hydraulic Tomography: Application at the Field Scale. Groundwater. https://doi.org/10.1111/gwat.12960.

Chaudhry, A., 2004. Oil Well Testing Handbook. Gulf Professional Publishing ISBN: 9780750677066.

Cheng, Y., Renner, J., 2018. Exploratory use of periodic pumping tests for hydraulic characterization of faults. Geophysical Journal International 212 (1), 543–565. https://doi.org/10.1093/gji/ggx390.

Copty, N.K., Findikakis, A.N., 2004. Stochastic analysis of pumping test drawdown data in heterogeneous geologic formations [Analyse stochastique des données de rabattement obtenues en pompages d'essai dans des formations géologiques hétérogènes]. Journal of Hydraulic Research 42 (sup1), 59–67. https://doi.org/10.1080/00221680409500048.

Despax, D., Dovis, R., Fedele, J.-M., & Martin, J.-P. (2004). Method and device for determining the quality of an oil well reserve. U.S. Patent, 6, 801–857.

Fokker, P.A., Renner, J., Verga, F., 2013. Numerical modeling of periodic pumping tests in wells penetrating a heterogeneous aquifer. American Journal of Environmental Sciences 9 (1), 1–13. https://doi.org/10.3844/ajessp.2013.1.13.

Fokker, P.A., Salina Borello, E., Serazio, C., Verga, F., 2012. Estimating reservoir heterogeneities from pulse testing. Journal of Petroleum Science and Engineering 86-87, 15–26. https://doi.org/10.1016/j.petrol.2012.03.017.

Fokker, P.A., Salina Borello, E., Verga, F., Viberti, D., 2018. Harmonic pulse testing for well performance monitoring. Journal of Petroleum Science and Engineering 162, 446–459. https://doi.org/10.1016/j.petrol.2017.12.053.

Fokker, P.A., Verga, F., 2011. Application of harmonic pulse testing to water-oil displacement. Journal of Petroleum Science and Engineering 79 (3–4), 125–134. https://doi.org/10.1016/j.petrol.2011.09.004.

Gringarten, A.C., Bourdet, D.P., Landel, P.A., Kniazeff, V.J., 1979. A comparison between different skin and wellbore storage typecurves for early-time transient analysis. SPE Annual Technical Conference and Exhibition. Las Vegas, Nevada: Society of Petroleum Engineers SPE8205MS. https://doi.org/10.2118/8205-MS.

Gringarten, A.C., 2008. From Straight Lines to Deconvolution: The Evolution of the State of the Art in Well Test Analysis. SPE Reservoir Evaluation & Engineering - SPE Reservoir Evaluation & Engineering 11 (01), 41–62. https://doi.org/10.2118/102079-PA.

Guiltinan, E., Becker, M.W., 2015. Measuring well hydraulic connectivity in fractured bedrock using periodic slug tests. Journal of Hydrology 521, 100–107. https://doi.org/10.1016/j.jhydrol.2014.11.066.

Hollaender, F., Hammond, P.S., Gringarten, A.C., 2002. Harmonic testing for continuous well and reservoir monitoring. In: Proceedings - SPE Annual Technical Conference and Exhibition. San Antonio, TX: Society of Petroleum Engineers (SPE). pp. 3071–3082. https://doi.org/10.2118/77692-MS.

Kuo, C.H., 1972. Determination of reservoir properties from sinusoidal and multirate flow tests in one or more wells. Society of Petroleum Engineers Journal 12 (06), 499–507. https://doi.org/10.2118/3632-PA.

Morozov, P.E., 2013. Harmonic testing of hydraulically fractured wells. In: Proceeding of 17th European Symposium on Improved Oil Recovery. St. Petersburg, Russia. pp. 16–18 April 2013.

Olarewaju, J.S., Lee, J.W., 1989. A Comprehensive Application of a Composite Reservoir Model to Pressure-Transient Analysis. SPE Reservoir Engineering 4(03). Society of Petroleum Engineers. https://doi.org/10.2118/16345-pa.

Renner, J., Messar, M., 2006. Periodic pumping tests. Geophysical Journal International 167 (1), 479–493. https://doi.org/10.1111/j.1365-246X.2006.02984.x.

Rochon, J., Jaffrezic, V., De La Combe, J.L.B., Azari, M., Roy, S., Dorffer, D., et al., 2008. Method and application of cyclic well testing with production logging. In: Denver, CO. Proceedings - SPE Annual Technical Conference and Exhibition 4. pp. 2376–2390. https://doi.org/10.2118/115820-MS.

Rosa, A.J., Horne, R.N., 1997. Reservoir description by well-test analysis by use of cyclic flow-rate variation. SPE Formation Evaluation 12 (04), 247–254. https://doi.org/10.2118/22698-PA.

Salina Borello, E., Fokker, P.A., Viberti, D., Espinoza, R., Verga, F., 2017. Harmonic-pulse testing for non-Darcy-effects identification. SPE Reservoir Evaluation and Engineering 20 (02), 486–501. https://doi.org/10.2118/183649-PA.S.

Salina Borello, E., Fokker, P.A., Viberti, D., Verga, F., Hofmann, H., Meier, P., Min, K.-B., Yoon, K., Zimmermann, G., 2019. Harmonic Pulse Testing for Well Monitoring: Application to a Fractured Geothermal Reservoir. Water Resources Research, pp. 2019. https://doi.org/10.1029/2018WR024029. 2018WR024029.

Sclumberger, 2016. Signature Quartz Gauges. Product sheet.

Sun, A.Y., Lu, J., Hovorka, S., 2015. A harmonic pulse testing method for leakage Detection in deep subsurface storage formations. Water Resources Research 51, 4263–4281. https://doi.org/10.1002/2014WR016567.

Verga, F., Viberti, D., Salina Borello, E., 2008. A new 3-D numerical model to effectively simulate injection tests. In: Rome: Society of petroleum engineers. 70th European Association of Geoscientists and Engineers Conference and Exhibition 2008: Leveraging Technology. Incorporating SPE EUROPEC 2008 Vol. 2. pp. 946–959. https://doi.org/10.2118/113832-MS.

Verga, F., Viberti, D., Salina Borello, E., Serazio, C., 2014. An effective criterion to prevent injection test numerical simulation from spurious oscillations. Oil & Gas Science and Technology – Revue d'IFP Energies Nouvelles 69 (4), 633–651. https://doi.org/10.2516/ogst/2013137.

Verga, F., Viberti, D., Salina Borello, E., 2011. A new insight for reliable interpretation and design of injection tests. Journal of Petroleum Science and Engineering 78 (1), 166–177. https://doi.org/10.1016/j.petrol.2011.05.002. Elsevier. (2011).

Viberti, D., 2016. Effective detrending methodology for harmonic transient pressure response. Geoingegneria Ambientale e Mineraria 149 (3), 55–62.

Viberti, D., Salina Borello, E., Verga, F., 2018. Pressure detrending in harmonic pulse test interpretation: When, why and how. Energies 11 (6), 1540. https://doi.org/10.3390/en11061540. MDPI.

Vinci, C., Steeb, H., Renner, J., 2015. The imprint of hydro-mechanics of fractures in periodic pumping tests. Geophysical Journal International 202 (3), 1613–1626. https://doi.org/10.1093/gji/ggv247.

Zhou, Y., Cardiff, M., 2017. Oscillatory hydraulic testing as a strategy for NAPL source zone monitoring: Laboratory Experiments. Journal of Contaminant Hydrology 200, 24–34. https://doi.org/10.1016/j.jconhyd.2017.03.005.